

**NATIONAAL LUCHT- EN RUIMTEVAARTLABORATORIUM**

NATIONAL AEROSPACE LABORATORY NLR

THE NETHERLANDS

NLR TP 97670 U

BOUNDARY INTEGRAL EQUATION METHODS FOR SCREEN PROBLEMS  
IN ACOUSTIC AND ELECTROMAGNETIC AEROSPACE RESEARCH

by

H. Schippers





NLR TECHNICAL PUBLICATION

TP 97670 U

BOUNDARY INTEGRAL EQUATION METHODS FOR SCREEN PROBLEMS  
IN ACOUSTIC AND ELECTROMAGNETIC AEROSPACE RESEARCH

by

H. Schippers

This paper has been prepared for publication in Journal of Engineering Mathematics.

Parts of this paper are based on:

- Investigations supported by the Netherlands Ministry of Defense and monitored by the Scientific Support Division of the Directorate of Material Royal Netherlands Airforce.
- Investigations carried out under a contract awarded by the Netherlands Agency for Aerospace Programs (NIVR), Contract number 02003N.

Division : Fluid Dynamics

Prepared : HS/ *JP* 19/3/98

Approved : BO/ *BO* 20/3/98

Completed : 970725

Order number : 113.609/526.003

Typ. : HS





## Summary

The paper describes the application of boundary integral equation methods to solve two problems in acoustic and electromagnetic aerospace research. The first problem is concerned with the structural-acoustic analysis of solar arrays of satellites. This analysis involves the solution of a boundary integral equation for determining the acoustic pressure jump across the solar panels. The solar panels are geometrically modelled as screens (i.e. open surfaces in three dimensional space). The second problem is related to the radar cross section prediction of engine inlets of fighter aircraft. The prediction requires the calculation of the scattered electromagnetic field when the inlet is illuminated by a radar beam. Engine inlets are modelled as three-dimensional perfectly conducting cavity-like screens. The scattered electric field is obtained by solving the Electric Field Integral Equation.



## Contents

<b>1</b>	<b>Introduction</b>	5
<b>2</b>	<b>Structural-acoustic analysis of solar arrays</b>	7
2.1	Mathematical formulation	7
2.2	Low frequency analysis	10
2.3	Two parallel solar panels	11
2.4	Estimates of acoustic energy	12
2.5	Numerical solution	15
2.6	Applications	18
<b>3</b>	<b>Radar Cross Section Calculations</b>	21
3.1	Mathematical formulation	22
3.2	Numerical solution	26
3.3	Accuracy of RCS predictions	28
3.4	Application to an engine inlet	29
3.5	Applicability of boundary integral equation methods	29
<b>4</b>	<b>Concluding remarks</b>	31
<b>5</b>	<b>References</b>	33

## 1 Introduction

In aerospace research, boundary integral equation methods are frequently used in various fields of applied mechanics for solving problems around thin obstacles. Geometrically, these thin obstacles are modelled as screens, i.e. open surfaces in three dimensional space. Since about 1950 many investigations have been performed to analyse the aerodynamic flow about (parts of) aircraft. In particular, lifting surface theory has been applied extensively to predict lift distributions on wings and propeller blades. Appropriate boundary integral equations were derived, and suitable numerical methods to solve these equations were developed.

Before the event of the digital computer, boundary integral equations were solved using basis functions with support on the whole boundary. Such global basis functions were advantageous from the point of view that the number of unknown coefficients was limited, so that the equations could be solved by the computational tools which were available at that time. In 1950 an important method for predicting the lift distribution on wings in the subsonic speed regime was presented by Multhopp (Ref. 1). In this method the wing is approximated by a plane sheet extending over the wing-platform. The mathematical problem is formulated in terms of an integral equation which relates the prescribed normal velocity on the wing surface with the pressure distribution over the wing surface. The pressure distribution is approximated by trigonometric basis functions satisfying the correct behaviour at the leading and trailing edges. The coefficients of the basis functions are determined by means of a collocation method. When digital computers became available, the convergence of this method was investigated by Zandbergen et al. in the 1960's. Lack of convergence was observed due to poor modelling of the singular behaviour of the kernel function. The method was improved by Zandbergen et al. in reference 2. Also, the range of applicability was extended to kinked wings (Ref. 3). The extension of this method to complex aircraft configurations (e.g. configurations with extended slats and flaps consisting of several segments) is, however, far from trivial because the global basis functions are defined on a single, simply connected domain that can be mapped onto a simple rectangular sheet. Instead, numerical methods were developed that use basis functions with local support. These so-called panel methods appear to be more tractable for treating complex geometries. Since the mid 1960's panel methods have been developed to the extent that they are routinely used in the aerospace industry. A drawback of these panel methods is that the computational cost is proportional to  $N^3$ , where  $N$  is the number of panels. However, due to the steady increase in computing power the limits on  $N$  move up every decade. On the currently available computers about 5000 panels are allowed. The major drawback of boundary integral equation methods in aerodynamics is that their range of applicability is restricted to linear inviscid potential flow, i.e. nonlinear

compressibility effects cannot be taken into account. As a consequence, transonic flows with shock waves cannot be treated by boundary integral equation methods. Therefore, from one of the major fields in aerospace research, viz. the analysis of aerodynamic flow around aircraft, there seem to be no pushing factors for further development of boundary integral equation methods. Instead, since about the mid 70's the investigations in this field have been addressed to the development of computational methods for the solution of non-linear flows governed by the full-potential equation, Euler equations and Navier-Stokes equations. However, new challenges have appeared for the development and application of boundary integral equation methods in other fields of aerospace research. In the present paper the following problems are discussed:

#### **Structural-acoustic analysis of solar arrays on satellites**

Modern spacecraft are equipped with large light-weight solar arrays. A solar array consists of a stack of solar panels, which is unfolded in orbit flight. During the launching phase the solar panels are folded into small packages and the distance between the panels is small. Then the solar array is exposed to severe dynamic loads which may affect the dynamic behaviour of the satellite. Therefore it is a prerequisite to analyse the dynamic behaviour of the solar arrays with the main structure of the satellite and to assess the effects of the vibrating air. The coupled structural-acoustic analysis of the solar array and the surrounding air involves the solution of a hyper-singular integral equation for determining the acoustic pressure jump across the solar panels. The panels are geometrically modelled as screens. The hyper-singular integral equation is numerically solved by a boundary element method, approximating the acoustic pressure jump by piecewise linear functions on a triangular surface grid.

#### **Radar Cross Section (RCS) calculations**

The development of prediction techniques for radar cross sections of aerospace platforms is motivated by the need to have tools available for both radar analysis and design of military aerospace vehicles. The vulnerability of fighter aircraft in several types of missions is among others determined by their detectability by radarsystems of which the frequency can vary typically from 0.1 to 94 GHz, corresponding with wavelengths of 3 meters to 3 millimeters. RCS predictions of aerospace platforms require the calculation of the fields scattered by the platform when illuminated by a plane electromagnetic wave (the radar beam). When illuminated nose-on, the engine inlets of aircraft account for approximately 90 % of the radar signature due to multiple reflections in these inlets. The interior surface of engine inlets is modelled as a three-dimensional perfectly conducting cavity-like screen. The scattered electric field is obtained by solving the Electric Field Integral Equation (EFIE) by applying the method of moments. In this method the local basis functions are defined by the classical Glisson-Rao vector functions on a triangular surface grid.

## 2 Structural-acoustic analysis of solar arrays

In this section a computational model is described to estimate the acoustic effect of the surrounding air on the harmonic vibration of a single solar panel (see figure 1) and an array of two parallel solar panels in close proximity (see figure 2). The sound pressure of the vibrating air is modelled by a boundary integral formula. The vibrating panel and the vibrating air are coupled by the acoustic coupling equation. The coupled analysis involves the solution of a hypersingular integral equation. For low frequencies, it will be shown that the vibrating air behaves as virtual mass which can be added to the mass of the panel. For the case of two parallel solar panels in close proximity, a structural-acoustic analysis is presented which is based on the modal analysis of a single solar panel. The acoustic energy of the vibrating air on the panels is estimated in terms of the small distance  $h$  between the two panels. The consequences of these energy estimates on the values of the lowest eigenfrequencies of two vibrating panels are discussed.

### 2.1 Mathematical formulation

The solar panels are modelled as plates (i.e. screens), smooth open surfaces in  $\mathbf{R}^3$ . The dynamics of a single harmonically vibrating panel is assumed to be governed by the weak formulation: find a displacement field  $\vec{w}$  such that

$$K(\vec{v}, \vec{w}) - \rho\lambda^2 M(\vec{v}, \vec{w}) = (\vec{n} \cdot \vec{v}, \mu) \quad (1)$$

for all possible displacement fields  $\vec{v}$ . Here,  $K(\vec{v}, \vec{w})$  and  $M(\vec{v}, \vec{w})$  denote respectively the first variation of the strain energy and the kinetic energy. In numerical calculations these bilinear forms will be modelled by four-noded finite shell elements (see section 2.5)). Furthermore,  $\rho$  denotes the density of the solar panels and  $\lambda$  the angular frequency. The right-hand side of (1) represents the the acoustic work due to the virtual normal displacement  $\vec{n} \cdot \vec{v}$  and the acoustic pressure jump

$$\mu = p^+ - p^-, \quad (2)$$

with  $p^+$  ( $p^-$ ) denoting the pressure on the upper (lower) side of the solar panel. Hence,

$$(\vec{n} \cdot \vec{v}, \mu) = \int_{\Omega} \vec{n} \cdot \vec{v} \mu \, dS, \quad (3)$$

where  $\Omega$  is the domain of the plate. When the solar array consists of multiple panels, equation (1) has to hold for all panels.

First consider the single solar panel (Fig. 1). If the panel vibrates in vacuum,  $\mu = 0$ . In this case (1) corresponds with a classical eigenvalue problem. The solution of this problem yields the vibration modes and the eigenfrequencies of the panel in vacuum. However, if the panel vibrates in air, the pressure jump  $\mu$  does not in general vanish. Below, an expression for  $\mu$  in terms of  $\vec{n} \cdot \vec{w}$  is derived, which changes (1) in a perturbed eigenvalue problem. The acoustics is governed by the Helmholtz equation. The sound pressure of the vibrating air satisfies the following boundary integral formula

$$p(\vec{r}) = - \int_{\Omega} \frac{\partial G}{\partial n'}(\vec{r}, \vec{r}') \mu(\vec{r}') dS', \quad \vec{r} \in \mathbf{R}^3 \setminus \Omega, \quad (4)$$

where  $G$  represents the fundamental solution of the Helmholtz equation in an infinite domain,

$$G(\vec{r}, \vec{r}') = \frac{e^{-jk|\vec{r}-\vec{r}'|}}{4\pi|\vec{r}-\vec{r}'|}, \quad \forall \vec{r} \neq \vec{r}', \quad (5)$$

with  $k$  the wave number ( $k = \lambda/c$  with  $c$  the speed of sound).

The vibrating panel and the vibrating air are coupled by the acoustic coupling equation

$$\frac{\partial p}{\partial n} = \rho_a \lambda^2 w_n, \quad (6)$$

where  $w_n = \vec{n} \cdot \vec{w}$  and  $\rho_a$  is the density of the air.

Application of this boundary condition to the boundary integral formula (4) yields the hypersingular integral equation

$$- \int_{\Omega} \frac{\partial^2 G}{\partial n \partial n'}(\vec{r}, \vec{r}') \mu(\vec{r}') dS' = \rho_a \lambda^2 w_n(\vec{r}), \quad \vec{r} \in \Omega, \quad (7)$$



or in operator notation

$$T\mu = \rho_a \lambda^2 w_n. \quad (8)$$

In equation (7), the integral  $\mathcal{f}$  is defined as a finite part integral in the sense of Hadamard. The mathematical aspects of the integral equation (7), as defined on screens in  $\mathbf{R}^3$ , have been studied in detail by Stephan (Ref. 4). In that paper it has been proved that the operator  $T$  defines a continuous mapping from  $\tilde{H}^s(\Omega)$  onto  $H^{s-1}(\Omega)$  for any real number  $s$ . Here  $\tilde{H}^s(\Omega)$  is defined as in reference 4: if  $V$  is a bounded domain with smooth boundary  $\Gamma$  and  $\Omega \subset \Gamma$ , then  $\tilde{H}^s(\Omega) = \{u \in H^s(\Gamma) : \text{supp } u \subset \Omega\}$ . The inverse of the operator  $T$  exists as a continuous mapping from  $H^{-1/2}(\Omega)$  onto  $\tilde{H}^{1/2}(\Omega)$ , (see Ref. 4, theorem 2.7), so that (8) yields the following expression for the pressure jump in terms of  $w_n$

$$\mu = \rho_a \lambda^2 T^{-1} w_n. \quad (9)$$

When this expression is substituted into (1) the following coupled differential boundary integral equation is obtained

$$K(\vec{v}, \vec{w}) - \rho \lambda^2 M(\vec{v}, \vec{w}) - \rho \epsilon \lambda^2 (v_n, T^{-1} w_n) = 0, \quad \epsilon = \frac{\rho_a}{\rho}. \quad (10)$$

Note that  $\epsilon$  has no physical dimension. For metallic plates  $\epsilon$  is so small that the last term in (10) may be neglected in the structural-acoustic analysis. For solar panels, however,  $\epsilon$  is of the order of 0.01, and it will be shown in this paper that then the vibrating air does have a non-negligible effect on the values of the eigenfrequencies.

Equation (10) defines a compactly perturbed eigenvalue problem. The problem depends in a nonlinear way on  $\lambda^2$ , due to the occurrence of  $\lambda$  in  $T$  by the Green function  $G$  via  $k = \lambda/c$ . Equation (10) can be solved by using an iteration process for each eigenfrequency: solve for  $i = 1, 2, 3, \dots$

$$K(\vec{v}, \vec{w}_i) - \rho \lambda_i^2 M(\vec{v}, \vec{w}_i) - \rho \epsilon \lambda_i^2 (v_n, T_{\lambda_i^{-1}}^{-1} w_{n,i}) = 0. \quad (11)$$

The dependence of  $T$  on  $\lambda$  is stressed by the notation  $T_\lambda$ . Initial values for the eigenmodes and eigenfrequencies are obtained by solving (10) in vacuum by taking  $\epsilon = 0$ . The eigenfrequencies in vacuum are used to evaluate  $T_{\lambda_0}$ . The convergence of this iteration process has been investigated in reference 5 for the lower eigenfrequencies, for which fast convergence was observed.

The numerical calculations are based on the simultaneous solution of differential equation (1) and boundary integral equation (8) using the following weak formulation: find non-trivial  $\vec{w} \in (H^1(\Omega))^3$ ,  $\mu \in \tilde{H}^{1/2}(\Omega)$  and  $\lambda \in \mathbf{R}^1$  such that

$$K(\vec{v}, \vec{w}) - \rho\lambda^2 M(\vec{v}, \vec{w}) - (\vec{n} \cdot \vec{v}, \mu) = 0, \quad (12)$$

$$- (\xi, \vec{n} \cdot \vec{w}) + \frac{1}{\rho_a \lambda^2} (\xi, T\mu) = 0, \quad (13)$$

for all  $\vec{v} \in (H^1(\Omega))^3$ ,  $\xi \in \tilde{H}^{1/2}(\Omega)$ . The bilinear form  $(\xi, T\mu)$  in (13) reads

$$(\xi, T\mu) = - \int_{\Omega} \int_{\Omega} \frac{\partial^2 G}{\partial n \partial n'}(\vec{r}, \vec{r}') \nu(\vec{r}') \xi(\vec{r}) dS' dS. \quad (14)$$

Equation (12) is discretized by finite elements and equation (13) by boundary elements.

The hypersingular integral operator is regularised through integration by parts, using the boundary conditions that  $\mu$  and  $\xi$  vanish along the edges of the plates (i.e. no pressure jump along  $\partial\Omega$ ) and the fact that  $G$  is the fundamental solution of the Helmholtz operator. According to reference 6, this leads to the following expression,

$$\begin{aligned} (\xi, T\mu) &= \int_{\Omega} \int_{\Omega} G(\vec{r}, \vec{r}') \langle \vec{n}_r \times \nabla_r \xi(\vec{r}), \vec{n}_{r'} \times \nabla_{r'} \mu(\vec{r}') \rangle dS' dS \\ &\quad - k^2 \int_{\Omega} \int_{\Omega} G(\vec{r}, \vec{r}') \mu(\vec{r}') \xi(\vec{r}) \langle \vec{n}_r, \vec{n}_{r'} \rangle dS' dS, \end{aligned} \quad (15)$$

where  $\langle \vec{a}, \vec{b} \rangle$  denotes the in-product between  $\vec{a}$  and  $\vec{b}$ . Note that (15) contains only weakly singular integrals.

## 2.2 Low frequency analysis

For low frequencies, the Green function  $G$  can be approximated by

$$G(\vec{r}, \vec{r}') = \frac{1}{4\pi|\vec{r} - \vec{r}'|} - \frac{jk}{4\pi} + \mathcal{O}(k^2). \quad (16)$$

When this approximation is substituted into equation (15), it follows that

$$\begin{aligned}
 (\xi, T\mu) &= \int_{\Omega} \int_{\Omega} \frac{1}{4\pi|\vec{r}-\vec{r}'|} \langle \vec{n}_r \times \nabla_r \xi(\vec{r}), \vec{n}_{r'} \times \nabla_{r'} \mu(\vec{r}') \rangle dS' dS \\
 &\quad - \frac{jk}{4\pi} \int_{\Omega} \int_{\Omega} \langle \vec{n}_r \times \nabla_r \xi(\vec{r}), \vec{n}_{r'} \times \nabla_{r'} \mu(\vec{r}') \rangle dS' dS + \mathcal{O}(k^2).
 \end{aligned} \tag{17}$$

Similarly, the operator  $T$  may be approximated by, compare (7) and (8),

$$T = T_0 - jkD_0 + \mathcal{O}(k^2), \tag{18}$$

where  $T_0$  and  $D_0$  are defined by the bilinear forms in the right hand side of (17). It can be proved that the operator  $T_0$  is positive definite on  $\tilde{H}^{1/2}(\Omega)$ . The inverse of this approximation for  $T$  reads

$$T^{-1} = T_0^{-1} + jkT_0^{-1}D_0T_0^{-1} + \mathcal{O}(k^2). \tag{19}$$

Upon using this, equation (10) becomes

$$K(\vec{v}, \vec{w}) - \rho\lambda^2 M(\vec{v}, \vec{w}) - \rho\epsilon\lambda^2 (\vec{n} \cdot \vec{v}, T_0^{-1} \vec{n} \cdot \vec{w}) + (j\lambda)^3 \frac{\rho\epsilon}{c} (\vec{n} \cdot \vec{v}, T_0^{-1} D_0 T_0^{-1} \vec{n} \cdot \vec{w}) = 0, \tag{20}$$

Note that the first term of (19) can be seen as virtual mass (of the vibrating air), which is added to the mass of the solar panel. The second term of (19) induces the last term in equation (20), which is proportional to  $\lambda^3$ . For low frequencies the contribution of this term to the perturbation of the eigenfrequencies is small.

### 2.3 Two parallel solar panels

For the case of two parallel solar panels (modelled as two rectangular plates  $\Omega_1$  and  $\Omega_2$ ), at a small distance  $h$  apart from each other (see figure 2), the mathematical formulation is adjusted by simply putting  $\Omega = \Omega_1 \cup \Omega_2$ . When the acoustic coupling equation (6) is applied to both plates  $\Omega_1$  and  $\Omega_2$  the following system of boundary integral equations is obtained,

$$\begin{aligned}
 T_{11}\mu_1 + T_{12}\mu_2 &= \rho_a \lambda^2 \vec{n} \cdot \vec{w}_1, \quad \text{on } \Omega_1, \\
 T_{21}\mu_1 + T_{22}\mu_2 &= \rho_a \lambda^2 \vec{n} \cdot \vec{w}_2, \quad \text{on } \Omega_2,
 \end{aligned} \tag{21}$$



where  $\mu_i$  and  $\vec{w}_i$  ( $i = 1, 2$ ) denote respectively the jump in the acoustic pressure and the displacement field on  $\Omega_i$ . The boundary integral operators  $T_{ij}$  are given by

$$T_{ij}\mu_j(\vec{r}) = - \int_{\Omega_j} \frac{\partial^2 G}{\partial n \partial n'}(\vec{r}, \vec{r}') \mu_j(\vec{r}') dS', \quad \vec{r} \in \Omega_i. \quad (22)$$

Observe that the integral operators  $T_{11}$  and  $T_{22}$  correspond with the operator  $T$  of (8). Hence

$$T_{11} = T_{22} = T. \quad (23)$$

The operators  $T_{12}$  and  $T_{21}$  model the acoustic effects that the plates have upon each other. The weak formulation (13) is used for the solution of (21). The bilinear form related to  $T_{12}$  is, see (15),

$$(\xi_1, T_{12}\mu_2) = \int_{\Omega_1} \int_{\Omega_2} G(\vec{r}, \vec{r}') \{ \langle \vec{n} \times \nabla \xi_1, \vec{n}' \times \nabla' \mu_2 \rangle - k^2 \xi_1 \mu_2 \langle \vec{n}, \vec{n}' \rangle \} dS' dS. \quad (24)$$

These integrals are of regular type, but their evaluation by means of numerical integration rules has to be carried out carefully, because the Green function  $G$  behaves as  $1/h$  if  $|\vec{r} - \vec{r}'|$  is minimal (i.e. when  $\vec{r}$  and  $\vec{r}'$  are opposite to each other). Appropriate quadrature formulas have been presented in reference 7. Obviously, the above formulation can be extended to a solar array consisting of an arbitrary number of panels.

#### 2.4 Estimates of acoustic energy

For a single vibrating panel the acoustic energy of the vibrating air on a solar panel is proportional to

$$\mathcal{A}_1 = \int_{\Omega} \vec{n} \cdot \vec{w} \mu dS, \quad \text{with} \quad \mu = \rho_a \lambda^2 T^{-1} \vec{n} \cdot \vec{w}. \quad (25)$$

Similarly, for two vibrating panels the acoustic energy is related to

$$\mathcal{A}_2 = \int_{\Omega_1 \cup \Omega_2} \vec{W} \cdot \vec{\mu} dS, \quad (26)$$

with

$$\vec{W} = \begin{pmatrix} \vec{n} \cdot \vec{w}_1 \\ \vec{n} \cdot \vec{w}_2 \end{pmatrix} \quad \text{and} \quad \vec{\mu} = \rho_a \lambda^2 Z^{-1} \vec{W}, \quad (27)$$

where  $Z$  corresponds with the matrix of operators on the left-hand side of equation (21),

$$Z = \begin{pmatrix} T_{11} & T_{12} \\ T_{21} & T_{22} \end{pmatrix}. \quad (28)$$

When the distance between the panels is large, there is no interaction between the panels ( $T_{12} = T_{21} = 0$  in equation (21)). Then,  $\mu_1 = \rho_a \lambda^2 T^{-1} \vec{n} \cdot \vec{w}_1$  and  $\mu_2 = \rho_a \lambda^2 T^{-1} \vec{n} \cdot \vec{w}_2$ . As a consequence, the acoustic energy corresponds with the energy of two single solar panels, i.e.

$$A_2 = \rho_a \lambda^2 \left( \int_{\Omega_1} \vec{n} \cdot \vec{w}_1 T^{-1} \vec{n} \cdot \vec{w}_1 dS + \int_{\Omega_2} \vec{n} \cdot \vec{w}_2 T^{-1} \vec{n} \cdot \vec{w}_2 dS \right). \quad (29)$$

For panels in close proximity, a first order expansion of  $T_{12}$  in terms of  $h$  has been derived in reference 8. It was shown that  $T_{12}$  may be approximated up to first order in  $h$  by

$$T_{12} = T - \frac{1}{2} h V, \quad (30)$$

where the operator  $V$  is related to the weak formulation of the Helmholtz equation, i.e.,

$$(\xi, V\mu) = \int_{\Omega_1} (\nabla_{s\mu} \cdot \nabla_s \xi - k^2 \xi \mu) dS, \quad (31)$$

with  $\xi = \mu = 0$  on the edge of  $\Omega_1$ . A similar relation holds for  $T_{21}$ . Equations (21), (23) and (30) can now be used to estimate the acoustic effects of in-phase vibration of the panels (given by  $\vec{w}_1 = \vec{w}_2 = \vec{w}$ ) and out-of-phase vibration (given by  $\vec{w}_1 = -\vec{w}_2 = \vec{w}$ ).

If the panels are vibrating in-phase, the pressure jumps over the panels can be approximated by

$$\mu_1 = \mu_2 = \frac{1}{2} \rho_a \lambda^2 (T^{-1} + \frac{h}{4} T^{-1} V T^{-1}) \vec{n} \cdot \vec{w}. \quad (32)$$

Then, the acoustic energy  $\mathcal{A}_2$  becomes for small values of  $h$ , compare (25),

$$\begin{aligned} \mathcal{A}_2 &= \rho_a \lambda^2 \left( \int_{\Omega_1} \vec{n} \cdot \vec{w} T^{-1} \vec{n} \cdot \vec{w} dS + \frac{h}{4} \int_{\Omega_1} \vec{n} \cdot \vec{w} T^{-1} V T^{-1} \vec{n} \cdot \vec{w} dS \right) \\ &= \mathcal{A}_1 + O(h). \end{aligned} \quad (33)$$

Comparison of this expression with (29) shows that, when the distance  $h$  between the panels tends to zero, the acoustic energy tends to half the value for two single solar panels (without interaction). For small values of  $h$ , the acoustic energy of two in-phase vibrating panels thus corresponds with the acoustic energy of a single solar panel with air on both sides but with half the value of the air density.

When the panels are vibrating out-of-phase it follows from (21), (23) and (30) that

$$\mu_1 = -\mu_2 = \rho_a \lambda^2 \frac{2}{h} V^{-1} \vec{n} \cdot \vec{w}. \quad (34)$$

Then the acoustic energy  $\mathcal{A}_2$  becomes for small values of  $h$ ,

$$\mathcal{A}_2 = \rho_a \lambda^2 \frac{4}{h} \int_{\Omega_1} \vec{n} \cdot \vec{w} V^{-1} \vec{n} \cdot \vec{w} dS, \quad (35)$$

which differs completely from the relation (33) for in-phase vibrating panels. Now the acoustic effects are dominated by the vibrating air between the panels, and the acoustic energy is inversely proportional to the distance  $h$ . When the panels vibrate out-of-phase, the air is pumped in and out of the gap between the panels, which causes a large energy transfer from the panels to the air in the gap. So far it has been assumed that the air could be treated as inviscid. For narrow gaps, however, the viscosity of the air cannot be neglected for out-of-phase vibration. A more sophisticated model (including effects of inertia, viscosity, compressibility and thermal conductivity) has been presented in reference 9. It was shown that the viscosity of the air results in a significant amount of damping when the distance between the panels becomes small.

## 2.5 Numerical solution

The structural analysis of the solar panels is based on Reissner-Mindlin theory for moderately thick plates. This theory assumes that the in plane displacements  $w_1$  and  $w_2$  have the form

$$w_1(x, y, z) = z\beta_1(x, y), \quad w_2(x, y, z) = z\beta_2(x, y) \quad (36)$$

and that the normal displacement  $w_3$  has the form

$$w_3(x, y, z) = w(x, y). \quad (37)$$

The strain energy and the kinetic energy associated with this displacement field have been given in reference 10. The strain energy reads

$$\mathcal{U} = \frac{1}{2}a(\vec{\beta}, \vec{\beta}) + \frac{1}{2}D\chi\kappa \int_{\Omega} |\nabla w + \vec{\beta}| dS, \quad (38)$$

where

$$a(\vec{\beta}, \vec{\beta}) = D \int_{\Omega} \left\{ \left( \frac{\partial\beta_1}{\partial x} + \nu \frac{\partial\beta_2}{\partial y} \right) \frac{\partial\beta_1}{\partial x} + \left( \nu \frac{\partial\beta_1}{\partial x} + \frac{\partial\beta_2}{\partial y} \right) \frac{\partial\beta_2}{\partial y} + \frac{(1-\nu)}{2} \left( \frac{\partial\beta_1}{\partial y} + \frac{\partial\beta_2}{\partial x} \right)^2 \right\} dS, \quad (39)$$

in which  $\nu$  is the Poisson ratio,  $D$  the flexural rigidity,  $\chi$  the shear modulus and  $\kappa$  the shear correction factor. The kinetic energy, including the effect of rotary inertia, is given by

$$\mathcal{V} = \frac{1}{2}\rho\lambda^2 \int_{\Omega} \left\{ \delta w^2 + \frac{1}{12}\delta^3(\beta_1^2 + \beta_2^2) \right\} dS, \quad (40)$$

in which  $\delta$  is the thickness of the plate. The bilinear forms  $K(\vec{v}, \vec{w})$  and  $M(\vec{v}, \vec{w})$  of equation (1) follow from the first variation of  $\mathcal{U}$  and  $\mathcal{V}$ , respectively. The cross-sectional rotations  $\beta_1, \beta_2$  and the normal displacement  $w$  are approximated by the four-noded  $C^0$  elements of Ref. 11. This

finite element approximation of equation (12) yields the following system of algebraic equations

$$(\mathcal{K} - \lambda^2 \mathcal{M})\vec{U} = \vec{F}_a. \quad (41)$$

The matrices  $\mathcal{K}$  and  $\mathcal{M}$  are respectively the stiffness and mass matrix of the solar array. The vector  $\vec{U}$  contains the nodal displacements. The load vector  $\vec{F}_a$ , due to the pressure jump  $\mu$ , is given by

$$\vec{F}_a = \mathcal{C}^T \vec{J} \quad (42)$$

in which  $\mathcal{C}$  is the matrix which couples the displacement degrees of freedom with the pressure jump degrees of freedom. The vector  $\vec{J}$  contains the nodal pressure jumps.

The boundary integral equation (13) is solved by a boundary element method on a triangular surface grid of which the nodes correspond with the nodes of the quadrilateral mesh of the structural four-noded  $C^0$  elements. The computational aspects of this boundary element method have been described in reference 7, where special attention has been given to the evaluation of singular and nearly singular integrals. For (13) the discrete system of equations becomes

$$\mathcal{T}\vec{J} = \rho_a \lambda^2 \mathcal{C} \vec{U}. \quad (43)$$

Substitution of (43) into equations (41) and (42) yields

$$(\mathcal{K} - \rho \lambda^2 (\mathcal{M} + \mathcal{M}_a))\vec{U} = 0, \quad (44)$$

with  $\mathcal{M}_a = \epsilon \mathcal{C}^T \mathcal{T}^{-1} \mathcal{C}$ . The direct solution of equation (44) has the disadvantage that the boundary element method annihilates the sparseness of the finite element matrices. This increases computational cost considerably. The number of degrees of freedom of the coupled structural-acoustic analysis can be reduced by introducing the structural eigenmodes of (41) in vacuum as a new basis. Let  $\vec{\phi}_i$  be the  $i$ -th structural eigenmode in vacuum. Then the displacement field is

approximated by

$$\vec{U} = \sum_{i=1}^n u_i \vec{\phi}_i \equiv \Phi \vec{u}, \quad (45)$$

where  $\Phi$  denotes the reduced basis of eigenmodes. Then equations (41) and (43) become

$$(\tilde{\mathcal{K}} - \lambda^2 \tilde{\mathcal{M}}) \vec{u} = \tilde{\mathcal{C}}^T \vec{J} \quad (46)$$

$$T \vec{J} = \rho_a \lambda^2 \tilde{\mathcal{C}} \vec{u} \quad (47)$$

where  $\tilde{\mathcal{K}} = \Phi^T \mathcal{K} \Phi$ ,  $\tilde{\mathcal{M}} = \Phi^T \mathcal{M} \Phi$  and  $\tilde{\mathcal{C}} = \mathcal{C} \Phi$ . Eliminate  $\vec{J}$  from equations (46)-(47) to obtain

$$(\tilde{\mathcal{K}} - \rho \lambda^2 (\tilde{\mathcal{M}} + \tilde{\mathcal{M}}_a)) \vec{u} = 0, \quad (48)$$

with

$$\tilde{\mathcal{M}}_a = \epsilon \tilde{\mathcal{C}}^T T^{-1} \tilde{\mathcal{C}}. \quad (49)$$

This approach leads to a reduced system of equations with dimension  $n$ , the number of eigenmodes in the reduced basis  $\Phi$ . This number must be taken sufficiently large to obtain accurate results for the lowest modes of the coupled analysis.

Inspection of (49) reveals that it is sufficient to determine the pressure jumps due to the eigenmodes in vacuum, i.e. to determine the matrix  $T^{-1} \tilde{\mathcal{C}} = T^{-1} \mathcal{C} \Phi$ .

For low frequencies the matrix  $\mathcal{M}_a$  can be approximated by, compare equation (20),

$$\mathcal{M}_a = \epsilon \mathcal{C}^T T_0^{-1} \mathcal{C} - j \lambda \frac{\epsilon}{c} \mathcal{C}^T T_0^{-1} \mathcal{D}_0 T_0^{-1} \mathcal{C}. \quad (50)$$

When the second term of (50) is neglected, the lowest eigenfrequency of equation (44) reads

$$\lambda^2 = \frac{\langle \mathcal{K} \vec{U}_1, \vec{U}_1 \rangle}{\langle \mathcal{M} \vec{U}_1, \vec{U}_1 \rangle + \langle \mathcal{M}_{a,0} \vec{U}_1, \vec{U}_1 \rangle} \quad (51)$$

where  $\vec{U}_1$  is the eigenmode belonging to the lowest eigenfrequency and  $\mathcal{M}_{a,0}$  represents the first term of (50). By the bijectivity of  $T_0$  and its positive definiteness, it follows that  $\langle \mathcal{M}_{a,0} \vec{U}_1, \vec{U}_1 \rangle > 0$ . From (51) it follows that the lowest eigenfrequency of the problem in air (44) will be smaller than the corresponding eigenfrequency of the problem in vacuum.

## 2.6 Applications

The computational model of the previous section has been applied to representative flat solar array panels. The solar panels are sandwich panels with different core and fairing properties. For the analysis the panels are modelled as monolithic plates having the same mass per unit area and bending stiffness. The basic properties of the panels and the surrounding air are given in table 1.

Table 1 Properties of solar panel and air

Length	1.675 m
Width	1.25 m
Thickness	0.001 m
Elasticity modulus	$4.5444 E^{+13} \text{ N/m}^2$
Poisson's ratio	0.3
Density	$1122.2 \text{ kg/m}^3$
Density of air	$1.2 \text{ kg/m}^3$
Speed of sound	340 m/s

The panels are simply supported supported along the short edges. The large edges are free. The computational mesh on a single panel consists of  $16 \times 16$  quadrilateral elements. The triangular grid for the numerical solution of equation (13) is obtained by subdividing each quadrilateral element into two parts.

The first and second eigenmode of the solar panel (with the above properties) in vacuum are displayed in figure 3. The eigenfrequencies of the first five eigenmodes in vacuum are given in the second column of table 2. The eigenfrequencies of the solar panel in air are computed using the iterative procedure as discussed in equation (11). The eigenfrequencies in vacuum are used as starting frequency for the evaluation of the matrix  $\mathcal{T}$  in equation (47). The first approximation (obtained with  $i = 1$  in (11)) and the converged values of the first five frequencies are given in the third and fourth column of table (2). It is observed that the first approximations are already very close to the converged values; for most frequencies an error less than one percent is obtained. Comparing the in-vacuum and in-air frequencies it is observed that for this configuration the air has a large influence on the dynamic behaviour of a single panel. The eigenfrequencies are shifted

downwards significantly, as could be expected since the panel experiences the air as an added mass (see equation (51)).

Table 2 Eigenfrequencies (in Hz) of a single panel in vacuum and in air

mode	in vacuum	1 <sup>st</sup> approx	in air
1	33.25	25.20	25.30
2	68.58	59.05	59.14
3	136.67	107.97	110.21
4	182.31	156.64	158.02
5	192.25	166.81	166.98

When two solar panels are in close proximity (Figure 2), an acoustic wave radiated from one panel will hit the other and therefore influences its dynamic behaviour. From equations (33) and (35) it follows that the influence will increase if the distance between the panels decreases. This is confirmed by figures 4 and 5, where the effects on the eigenfrequencies are shown for the first and second pair of eigenmodes. A pair of eigenmodes consists of the two cases where the panels vibrate in-phase and out-of-phase, in each case with the same eigenmode per panel. It appears from figures 4 and 5 that the panels do not influence each other when the distance is large. Both in-phase and out-of-phase they have the same frequency, which is equal to the eigenfrequency of the single panel in air (see the fourth column of table (2)). This could be expected from the mathematical formulation (see equation (29)).

For small gap width  $h$  the effects on the eigenvalues are completely different for in-phase vibration and out-of-phase vibration, as could be expected from equations (33) and (35). The in-phase vibrating panels will feel only the air on one side of the panel. From equation (33) it follows that the acoustic energy of two in-phase vibrating panels corresponds with the acoustic energy of a single solar panel with air on both sides but with half the value of the density. As a consequence, the value of  $\langle \mathcal{M}_a U_1, U_1 \rangle$  in (51) for two panels should converge to half the value for a single solar panel. According to (50) and (51), for small values of  $h$ , the frequencies of two in-phase vibrating panels should converge to the frequency of a single solar panel with air on both sides but with half the value of its density. The first two eigenfrequencies of the latter problem have been calculated to be 28.45 Hz and 63.45 Hz. Inspection of figures 4 and 5 reveals that the eigenfrequencies of the in-phase vibrating panels converge correctly to these limit values.

For two out-of-phase vibrating panels (close to each other) the acoustic energy is inversely proportional to the distance  $h$ , as follows from equation (35). As a consequence, the value of



$\langle \mathcal{M}_a U_1, U_1 \rangle$  for two out-of-phase panels tends to  $\infty$  as  $h$  tends to zero. As follows from (51), for small values of  $h$ , the eigenfrequencies of two out-of-phase vibrating panels should converge to zero. This is established by the results of figure 4.

### 3 Radar Cross Section Calculations

Radar Cross Section (RCS) predictions of aerospace platforms are essential to assess their visibility under radar surveillance. This requires the calculation of the electromagnetic field scattered by the platform when illuminated by a plane electromagnetic wave (the incident radar beam). In this section, scattering mechanisms which contribute to the RCS of a typical fighter aircraft are discussed. These scattering mechanisms are depicted schematically in figure 6.

The simplest scattering mechanism is single reflections. When the incident radar beam hits the (perfectly conducting) aircraft surface it is scattered in a narrow beam around the specular direction. Single reflections dominate the RCS when the direction of the incident beam is about normal to large parts of the aircraft surface. This usually occurs only for small intervals about certain specific observation angles. After a single reflection the beam can hit the object again, giving rise to double reflections, triple reflections or even multiple reflections. Double and triple reflections largely contribute to the RCS when the object contains dihedral and trihedral corners; they often dominate the RCS over large intervals of observation angles. In the design of the U.S. advanced tactical fighter aircraft, blending at the wing-fuselage intersection has been applied in order to remove scattering due to double reflections. As to the external aircraft surface, it usually suffices to take up to triple reflections into account. However, when the beam enters a large cavity, such as the engine inlet of the aircraft, it can be reflected manifold (multiple reflections) before it leaves the cavity. The number of reflections depends strongly on the angle under which the beam enters, and on the geometry of the inlet. This so-called resonance phenomenon is responsible for a very large contribution to the radar signature of an aircraft when illuminated nose on.

The last scattering mechanism of importance is edge diffraction. When the incident radar beam hits a sharp edge (such as the leading or trailing edge of the wing) it is scattered in all directions. For specific polarizations of the incident beam, it is also possible that a wave is induced which runs over the aircraft surface until it is scattered by another edge. These so-called travelling waves can occur for example between the leading and the trailing edge of the wing. The edge diffraction phenomenon generally contributes less to the RCS than the aforementioned mechanisms, but for some angles can occasionally become the dominant contribution.

In reference 12 a high frequency prediction model (based on physical and geometrical optics) has been described to determine the scattered waves reflected from the external aircraft surface. This model, however, is not suitable for RCS calculations of engine inlets in the resonance regime, where the dimension of the inlet aperture is of the same order as the wavelength ( $\lambda$ ) of the incident

electromagnetic field. For that reason, many research investigations are going on, worldwide, to predict the RCS of the multiply reflected waves in the engine inlet by boundary integral equation methods. In the present paper the applicability of such methods is discussed. The interior surface of the engine inlets is modelled as a three-dimensional perfectly conducting cavity-like screen. The scattered electric field is obtained by numerically solving the Electric Field Integral Equation (EFIE), using the method of moments.

### 3.1 Mathematical formulation

The electromagnetic fields satisfy the Maxwell equations and appropriate boundary conditions. In a homogeneous source-free region the electromagnetic fields around a three dimensional object (with boundary  $S$ ) can be represented by the Stratton-Chu boundary integral formulas (Ref. 13) in terms of the tangential and normal components of the total electromagnetic field (denoted by  $\vec{E}^T, \vec{H}^T$ ) on the object surface. The formula for the scattered electric field  $\vec{E}^s$  reads

$$\vec{E}^s(\vec{r}) = \int_S \{-j\omega\mu(\hat{n} \times \vec{H}^T)G + (\hat{n} \times \vec{E}^T) \times \nabla G + (\hat{n} \cdot \vec{E}^T)\nabla G\} dS, \quad \forall \vec{r} \notin S. \quad (52)$$

A similar formula holds for the scattered magnetic field  $\vec{H}^s$ ,

$$\vec{H}^s(\vec{r}) = \int_S \{j\omega\epsilon(\hat{n} \times \vec{E}^T)G + (\hat{n} \times \vec{H}^T) \times \nabla G + (\hat{n} \cdot \vec{H}^T)\nabla G\} dS, \quad \forall \vec{r} \notin S. \quad (53)$$

Here,  $\hat{n}$  is the outward normal to  $S$ ,  $\omega$  the angular frequency of the electromagnetic field,  $\mu$  the permeability of the free space ( $\mu = 4\pi 10^{-7}$ ) and  $\epsilon$  is the permittivity of the free space ( $\epsilon = 10^{-9}/36\pi$ ), The Green function  $G$  represents the fundamental solution of the Helmholtz equation (see equation (5)). The wave number  $k$  in (5) is given by  $k = \omega\sqrt{\epsilon\mu} = 2\pi/\lambda$ , with  $\lambda$  the wavelength of the incident field.

The integral formulations (52) and (53) can be derived from the vector Helmholtz equations using a vector equivalent of Green's second identity (see e.g. Ref. 14). The vector operations in (52) and (53) are to be performed in the source coordinates.

For RCS calculations the electromagnetic field scattered by the object has to be determined, due to a plane wave (with direction vector  $\hat{k}^i$ ) illuminating the object. With the incident plane wave an electric field is associated with direction  $\hat{e}^i$  and magnitude  $E_0$ . The incident electric and magnetic

fields are specified as:

$$\vec{E}^i = \hat{e}^i E_0 e^{-ik\hat{k}^i \cdot \vec{r}}, \quad \vec{H}^i = \sqrt{\epsilon/\mu} \hat{k}^i \times \vec{E}^i. \quad (54)$$

The total electromagnetic field in the domain outside the scattering object is written as the sum of the incident field and the scattered field,

$$\vec{E}^T = \vec{E}^i + \vec{E}^s, \quad \vec{H}^T = \vec{H}^i + \vec{H}^s. \quad (55)$$

The tangential and normal components of the surface fields can be interpreted as electric and magnetic surface currents ( $\vec{J}$ ,  $\vec{M}$ ) and surface charge densities ( $\rho$ ,  $\rho_m$ )

$$\vec{J} = \hat{n} \times \vec{H}^T, \quad (56)$$

$$\vec{M} = -\hat{n} \times \vec{E}^T, \quad (57)$$

$$\rho = \epsilon \hat{n} \cdot \vec{E}^T, \quad (58)$$

$$\rho_m = \mu \hat{n} \cdot \vec{H}^T. \quad (59)$$

The electric and magnetic surface charge densities can be rewritten invoking the conservation of charge by using the continuity equations

$$\nabla \cdot \vec{J} + j\omega\rho = 0,$$

$$\nabla \cdot \vec{M} + j\omega\rho_m = 0.$$

When these expressions are substituted into equations (52) and (53) it follows that

$$\vec{E}^s(\vec{r}) = \int_S \left\{ -j\omega\mu \vec{J} G - \vec{M} \times \nabla G - \frac{1}{j\omega\epsilon} (\nabla \cdot \vec{J}) \nabla G \right\} dS, \quad \forall \vec{r} \notin S, \quad (60)$$

$$\vec{H}^s(\vec{r}) = \int_S \left\{ -j\omega\epsilon \vec{M} G + \vec{J} \times \nabla G - \frac{1}{j\omega\mu} (\nabla \cdot \vec{M}) \nabla G \right\} dS, \quad \forall \vec{r} \notin S. \quad (61)$$

For the special case of a metallic object (i.e. a perfect electric conductor), the tangential components of the total electric surface field (and thus also the magnetic surface currents) and the magnetic

surface charge density are zero,

$$\hat{n} \times \vec{E}^T = -\vec{M} = 0, \quad (62)$$

$$\rho_m = 0. \quad (63)$$

Then the boundary integral formulas (60) and (61) reduce to

$$\vec{E}^s(\vec{r}) = \int_S \left\{ -j\omega\mu\vec{J}G - \frac{1}{j\omega\epsilon}(\nabla \cdot \vec{J})\nabla G \right\} dS, \quad \forall \vec{r} \notin S \quad (64)$$

$$\vec{H}^s(\vec{r}) = \int_S \vec{J} \times \nabla G dS, \quad \forall \vec{r} \notin S. \quad (65)$$

Substitution of (55) and (64) in the boundary condition (62) yields the electric field integral equation (EFIE)

$$\hat{n} \times \int_S \left\{ j\omega\mu\vec{J}G + \frac{1}{j\omega\epsilon}(\nabla \cdot \vec{J})\nabla G \right\} dS = \hat{n} \times \vec{E}^i. \quad (66)$$

The magnetic field integral equation (MFIE) follows from (65) and applying the boundary condition (56),

$$\vec{J} = \hat{n} \times \vec{H}^T = \hat{n} \times \vec{H}^i + \hat{n} \times \int_S \vec{J} \times \nabla G dS + \frac{1}{2}\vec{J}. \quad (67)$$

The last term in (67) follows from the jump relations of classical potential theory. This equation subsequently reduces to

$$\frac{1}{2}\vec{J} - \hat{n} \times \int_S \vec{J} \times \nabla G dS = \hat{n} \times \vec{H}^i. \quad (68)$$

This is the general form of the MFIE, which is valid only for closed surfaces. For screens the EFIE has to be used. Since engine inlets of fighter aircraft are usually geometrically modelled as cavity-like screens, computational tools are being developed for the numerical solution of (66). The solution is obtained from a weak formulation of (66), which follows from multiplying (66) by a tangential test function  $\vec{W}$ . Then, the following weak formulation can be derived: find the complex surface current vector  $\vec{J} \in \vec{H}_{div}^{-1/2}(S)$ , with the solution space as presented in reference

4, such that

$$\frac{j}{\omega\epsilon} \int_S \int_S \{k^2 \vec{J} \cdot \vec{W} G - (\text{div} \vec{J})(\text{div}' \vec{W}') G\} dS' dS = \int_S \vec{E}^i \cdot \vec{W}' dS, \quad (69)$$

for all  $\vec{W}' \in \tilde{H}_{\text{div}}^{-1/2}(S)$ . Equation (69) describes the behaviour of the surface current on the object surface, as induced by the incident electromagnetic field  $\vec{E}^i$ . Once a solution of (69) has been found, the scattered electric field can be determined using the Stratton-Chu representation formula (64), or its far field asymptotic approximation.

When the object  $S$  represents a screen, it contains a boundary edge, which is denoted by  $\partial S$ . Let  $\vec{\nu}$  be the unit normal along  $\partial S$ , in the tangent plane to  $S$ . Along  $\partial S$  the normal component  $\vec{\nu} \cdot \vec{J}$  may not jump. Hence, for screens it is required that

$$\vec{\nu} \cdot \vec{J} = 0, \quad \text{along } \partial S. \quad (70)$$

Mathematical aspects, such as existence, uniqueness and regularity of solutions, of (69) for screen problems have been discussed in reference 15.

In section 3.3 the accuracy of the numerical solutions of (69) is assessed by comparing the results with the outcome of two-dimensional models. To this end, consider a scatter problem in two-dimensional space for the case where the object has no variation in  $z$ -direction. Let  $\Gamma$  be the two-dimensional cross section boundary of the object. Then the Electric Field Integral Equation (69) can be reduced to two independent scalar equations: one for Transverse Magnetic ( $TM^z$ ) polarization (where the direction of the incident electric field  $\vec{E}^i$  is aligned with the  $z$ -axis), and one for Transverse Electric ( $TE^z$ ) polarization (where the direction of the incident magnetic field  $\vec{H}^i$  is aligned with the  $z$ -axis).

For  $TM^z$  polarization the weak formulation reads: find the current  $J \in H^{-1/2}(\Gamma)$  such that

$$\frac{\omega\mu}{4} \int_{\Gamma} \int_{\Gamma} \psi(\vec{\rho}) J(\vec{\rho}') H_0^{(2)}(k|\vec{\rho} - \vec{\rho}'|) d\Gamma' d\Gamma = \int_{\Gamma} E_z^i(\vec{\rho}) \psi(\vec{\rho}) d\Gamma, \quad (71)$$

for all  $\psi \in H^{-1/2}(\Gamma)$ .

For  $TE^z$  polarization the weak formulation reads: find  $J \in H_0^{1/2}(\Gamma)$  such that

$$\frac{1}{4\omega\epsilon} \int_{\Gamma} \int_{\Gamma} \{k^2(\vec{c}(\vec{\rho}) \cdot \vec{c}(\vec{\rho}'))\psi(\vec{\rho})J(\vec{\rho}') - \frac{d\psi(\vec{\rho})}{dc} \frac{dJ(\vec{\rho}')}{dc}\} H_0^{(2)}(k|\vec{\rho} - \vec{\rho}'|)d\Gamma'd\Gamma = \int_{\Gamma} E_c^i(\vec{\rho})\psi(\vec{\rho})d\Gamma, \quad (72)$$

for all  $\psi \in H_0^{1/2}(\Gamma)$ .

Here  $H_0^{(2)}$  the Hankel-function of the second kind,  $\vec{c}$  the unit tangential vector along the boundary  $\Gamma$ ,  $\vec{\rho}$  a points on the boundary  $\Gamma$ ,  $E_z^i$  the  $z$ -component of the incident electric field, and  $E_c^i$  the tangential component of the incident electric field.

When the boundary  $\Gamma$  is not closed, the magnetic current  $J$  in equation (72) has to vanish at the end-points of the boundary. This criterion corresponds with requirement (70) for screens in three dimensional space.

### 3.2 Numerical solution

To obtain a solution of the electric field integral equation (69) through the Method of Moments a finite set of basisfunctions  $\vec{J}_n$  is defined and the current  $\vec{J}$  is approximated by a linear combination of them:

$$\vec{J} = \sum_n I_n \vec{J}_n \quad (73)$$

where  $I_n$  are constants to be determined. The basisfunctions are defined by the classical Glisson-Rao vector functions on a triangular surface grid (see Ref. 16). By inserting the representation (73) into the EFIE (69) and taking the testfunctions equal to the basisfunctions, a system of linear equations is obtained of the form

$$ZI = V. \quad (74)$$

The elements of the impedance matrix  $Z$  are given explicitly by

$$Z_{mn} = \frac{j}{\omega\epsilon} \int_S \int_S \{k^2 \vec{J}_m \cdot \vec{J}_n G - (\text{div} \vec{J}_m)(\text{div}' \vec{J}_n) G\} dS' dS, \quad \forall(m, n). \quad (75)$$

The voltage vector  $V$  is given by

$$V_m = \int_S \vec{E}^i \cdot \vec{J}_m dS, \forall m. \quad (76)$$

The Glisson-Rao basisfunctions were selected because of their applicability to a general class of geometries and for reasons of accuracy and efficiency (see also Ref. 16). These basisfunctions have local support on a pair of triangles sharing a common edge so that the inner (respectively outer) integration on the right-hand side of expression (75) is restricted to the support of  $\vec{J}'_n$  (respectively  $\vec{J}_m$ ) only. Thus the double integral in (75) involves at most four triangles. Different types of quadrature rules are applied to calculate (75), depending on the required integration accuracy. The Glisson-Rao basis-functions have a continuous normal component when crossing the common edge. The unknowns  $I_n$  in (73) are attached to common edges. When the scattering object defines a screen, edges of triangular patches have no neighbouring counterpart along the boundary  $\partial S$ . At these edges  $I_n = 0$  according to (70).

The computational model based on the above approach is called EFIE3D. For objects having (various) geometrical symmetries, the impedance matrix  $Z$  has a specific symmetric structure and only part of the matrix has to be computed. Let  $N$  be the dimension of the impedance matrix  $Z$  and  $p$  the number of symmetries. The computational cost of the EFIE3D model consists of three contributions:

- The cost of evaluating the impedance matrix; proportional to  $N^2/p$ .
- The cost of the Lower-Upper factorization; proportional to  $N^3/p^2$ .
- The cost of the remaining computations; at most proportional to  $N^2/p$ .

These estimates are valid only for large values of  $N$ .

The two-dimensional electric field integral equations (71) and (72) have been solved numerically using a boundary element Galerkin method. The boundary  $\Gamma$  of the object is partitioned into a number of segments and the electric currents are approximated by local functions on the boundary. In equation (71) the basis and testfunctions are taken piecewise constant, whereas they are taken piecewise linear in equation (72). This numerical approach has resulted in the EFIE2D computational model.



### 3.3 Accuracy of RCS predictions

The RCS of an object is defined as

$$\sigma = \lim_{r \rightarrow \infty} 4\pi r^2 \frac{|\vec{E}^s|^2}{|\vec{E}^i|^2}, \quad (77)$$

where  $r$  is the distance from object to observer. The unit of  $\sigma$  is area, usually in square meters, or it may be non-dimensional by dividing by wavelength squared,  $\sigma/\lambda^2$ . When the transmitter and receiver are at the same location, the RCS is usually referred as monostatic. It is referred as bistatic when the two are at different locations.

In order to assess the accuracy of the RCS predictions the EFIE3D model has been applied to a rectangular inlet with length  $10\lambda$ , width  $2\lambda$  and height  $2\lambda$ . The geometry of this inlet is shown in figure 7. The calculations have been carried out on uniform triangular surface grids using planar symmetry about the planes  $y = 0$  and  $z = 0$ . The surface grids are obtained as follows. First, a uniform rectangular grid is generated with mesh-size  $h$ . Subsequently, each quadrilateral element is divided into two triangular elements.

The accuracy of the computed RCS is assessed in two ways: i) by comparing the RCS results with the results of the EFIE2D model for an infinite rectangular inlet (cross section  $10\lambda \times 2\lambda$  extending from  $z = -\infty$  to  $z = +\infty$ , and ii) by refining the grid.

In figure 8 the RCS predictions of the EFIE3D model are compared with the predictions of the EFIE2D model. The 3D calculations have been carried out on the uniform triangular grid with a characteristic meshsize of  $h = \lambda/7$ . It is observed that the three dimensional results display the same scattering characteristics as do the two dimensional results. For  $TM^z$ -polarization the scattering of the 3D inlet and the 2D inlet are expected to agree because the direction of the incident electric field is parallel to the  $z$ -axis. Therefore the horizontal plates of the 3D inlet will not contribute to the RCS, because the right-hand side of (66) vanishes at these plates. This is confirmed by figure 8, although in the interval between  $\phi = 10^\circ$  and  $\phi = 60^\circ$  the RCS of EFIE 3D is slightly higher, due to the rather coarse sampling that has been used in the EFIE3D model. For  $TE^z$ -polarization the higher values of the 3D RCS predictions in this interval are mainly due to the contributions of the horizontal plates of the 3D inlet which are not present in the 2D computations.

The convergence of the 3D RCS predictions is assessed in figure 9, where results are presented of EFIE3D calculations on uniformly triangular discretizations with meshsizes of  $h = \lambda/3$ ,  $h = \lambda/5$  and  $h = \lambda/7$ , respectively. This figure apparently reveals that the triangular discretization with meshsize  $h = \lambda/3$  is too coarse to get an accurate RCS prediction at the open side of the inlet. The RCS predictions of the EFIE3D model improve when the mesh is refined. For a discretization with meshsize  $h = \lambda/7$  reliable RCS results are obtained.

### 3.4 Application to an engine inlet

The EFIE3D model has been applied to analyse the RCS of a curved engine inlet with a square entrance (Fig. 10). It has a curved axis of 4 meters length. The surface has been approximated by 4454 triangular patches (Fig. 10). The coordinate system (see figure 10) has been chosen such that one looks straight into the inlet at  $\phi = 0^\circ$ ,  $\theta = 90^\circ$ . At a frequency of 1.5 GHz (wavelength 20 cm) and an illumination angle of  $\phi = -25^\circ$ ,  $\theta = 90^\circ$ , the scattered electric field has been computed. In figure 11 the bistatic RCS characteristics are displayed with the observer in the  $xy$ -plane (i.e.  $\theta = 90^\circ$ ). The maximum around  $\phi = 155^\circ$  (the "forward lobe") arises from the scattered electric field compensating for the incident field. The peak near  $\phi = -165^\circ$  is due to single reflection of the incident waves. The bistatic cross section is rather small in the vicinity of  $-90^\circ$  or  $+90^\circ$  as the receiver direction is perpendicular to the direction of the incident field. Thus the shape of the inlet is such that there is hardly any scattering in these directions. Most of the scattering in this scattering range is due to diffraction on the sharp edges at the top and bottom of the inlet entrance. In the neighbourhood of  $\phi = 0^\circ$  the scattering cross section has a smoother behaviour due to the fact that waves coming out of the inlet have multiply reflected inside. The local maximum in the vicinity of  $\phi = \pm 25^\circ$  is caused mainly by multiple reflection at the inlet wall and the inlet face: one can "see" the inlet face and the local maxima of the surface current from this point of view.

### 3.5 Applicability of boundary integral equation methods

The applicability of the computational model as described in section 3.2 is frequency limited because of the numerical approach involved in the model and due to computer hardware limitations. On the currently available supercomputers the model can be applied to engine inlets of fighter aircraft up to radar frequencies of about 1 GHz. Many research efforts are aimed at increasing the applicability of boundary integral equation methods to higher frequencies. A promising approach appears to be the application of entire domain functions (see e.g. Ref. 17). These functions have global support instead of local support on triangular patches. It is foreseen that the dimension of the impedance matrix will then decrease, so that the integral equation methods will become applicable to higher frequencies. Similar entire domain functions were used by Multhopp (Ref. 1)



in the 1950's to predict the lift distribution on wings in the subsonic speed regime. The use of these functions was advantageous from the point of view that a small system of equations results, which could be solved by the computational means available at that time. The mathematical formulation of entire domain functions requires that the surface can be mapped onto a simple rectangular computational domain. Therefore, geometries like engine inlets have to be decomposed into subdomains, in such a way that each part can be represented by a continuous mapping. E.g. the surface of the engine inlet of figure 10 has to be decomposed into two parts, one part describing the circumferential boundary and a second part describing the rear face. Then, at each part appropriate entire domain functions are defined. Along the common edges of the subdomains the entire domain functions have to match. In general, this is a difficult task. Therefore, it is recommended to apply the classical Glisson-Rao basis functions (with local support) only in the neighbourhood of the edges, and to apply the entire domain functions elsewhere. This approach involves the specification of so-called cut-off functions that define the region where the local basis functions are used. At the National Aerospace Laboratory NLR the applicability of this approach is being investigated for the numerical solution of the two-dimensional electric field integral equations (71) and (72). It appears that the computation of the coefficients of the impedance matrix requires the numerical calculation of integrals with strongly oscillating integrands. Integration techniques as developed in the 1960's (e.g. Ref. 18) may be useful to decrease the computational costs for the calculation of the impedance matrix.

An alternative approach to increase the applicability of boundary integral equation methods to higher frequencies is the development of parallel algorithms for the solution of (69) and the implementation on parallel hardware architectures (see e.g. Ref. 19).

#### 4 Concluding remarks

In the present paper two problems in aerospace research have been addressed which involve the numerical solution of boundary integral equations on screens. The first problem is concerned with the structural-acoustic analysis of light-weight solar array panels, which are geometrically modelled as screens. The second problem is related to RCS predictions of engine inlets of fighter aircraft, where the interior surface of the engine inlet is modelled as a perfectly conducting cavity-like screen.

The acoustic effects of the surrounding air on the dynamic behaviour of solar arrays have been analysed for two cases: a single solar panel and an array consisting of two parallel solar panels in close proximity. For low frequencies, the single solar panel experiences the air as an added mass. As a consequence, the computed eigenfrequencies are shifted downwards significantly. For two parallel panels, estimates for the acoustic energy of the vibrating air have been derived in terms of the small distance  $h$  between the two panels. For  $h$  tends to zero, the acoustic energy of two in-phase vibrating panels tends to half the value for two single solar panels (without interaction). For two out-of-phase vibrating panels the acoustic energy is inversely proportional to the distance  $h$ , when  $h$  tends to zero. Inspection of the computed eigenfrequencies has revealed that the behaviour of the lowest eigenfrequencies is consistent with these energy estimates for small values of  $h$ .

RCS predictions of engine inlets of fighter aircraft are obtained by a boundary integral equation method for the solution of the electric field integral equation. The accuracy of RCS predictions has been assessed for a rectangular inlet with length  $10\lambda$ , width  $2\lambda$  and height  $2\lambda$ . From the results of section 3.3 it is obvious that multiple reflections inside engine inlets can only be accurately modelled by using surface grids with at least seven patches per wavelength in one direction (i.e.  $h = \lambda/7$ ). The boundary integral equation method has been applied to analyse the RCS of a curved engine inlet with a square entrance. At the open side the computed RCS shows broad smooth lobes, which are caused by multiple reflections at the inside wall of the inlet.

The numerical methods, to solve the boundary integral equations in the above problems, use local basis functions on triangular surface grids. They require the generation of a complex-valued matrix. The dimension  $N$  of this matrix is proportional to the square of the frequency. The computational cost for solving the equations is proportional to  $N^3$ . For objects which are large with respect to the wavelength, the numerical methods using these local basis functions become intractable, because the required computational resources become too large. In particular, for RCS calculations the described boundary integral methods can only be applied to engine inlets of



fighter aircraft up to radar frequencies of about 1 GHz on the currently available supercomputers. For higher frequencies the computation times and the required computer storage become too large. Therefore, many research investigations are going on, worldwide, to increase the applicability of boundary integral equation methods to higher frequencies. Instead of using local basis functions, there is renewed interest in the application of appropriate basis functions with global support, which were also used to solve boundary integral equations before the availability of digital computers. The aim of these investigations is to decrease the dimension of the matrix of influence coefficients and to lower the required computer storage. Integration techniques for the numerical calculation of integrals with strongly oscillating integrands may be useful to decrease the computational costs for evaluating the influence coefficients.

### **Acknowledgements**

Some parts of this investigation were supported by the Netherlands Ministry of Defense and monitored by the Scientific Support Division of the Directorate of Material Royal Netherlands Airforce, other parts were supported by the Netherlands Agency for Aerospace Programs (NIVR). The EFIE3D computational model was developed in a cooperative program with DASA-MA (Munich).

The author would like to thank his colleagues F.P. Grooteman and F. Klinker for carrying out parts of the calculations. The author is grateful to J. van der Vooren for his advices in preparing this paper.

## 5 References

1. H. Multhopp, *Methods for calculating the lift distribution of wings (subsonic lifting surface theory)*, Report no. Aero 2353 R.A.E. (1950).
2. P.J. Zandbergen, T.E. Labrujere and J.G. Wouters, *A new approach to the numerical solution of the equation of subsonic lifting surface theory*, NLR TR G.49 (1967), National Aerospace Laboratory NLR.
3. T.E. Labrujere and P.J. Zandbergen, On the application of a new version of lifting surface theory to non slender and kinked wings, *Journal of Engineering Mathematics*, 7 (1973) 85-96.
4. E.P. Stephan, Boundary integral equations for screens in  $\mathbf{R}^3$ , *Integral Equations and Operator Theory* 10 (1987), 236-257.
5. F.P. Grooteman and H. Schippers, *Coupled analysis in acoustics on the dynamical behaviour of solar arrays*, NLR TP 94268 (1994) National Aerospace Laboratory NLR.
6. J.C. Nedelec, Approximation par potentiel de double conche du problème de Neumann Exterieur, *C.R. Acad. Sci. Paris, Ser. A*, 286 (1977), 616-619.
7. H.T. Koelink, H. Schippers, J.J. Heijstek and J.J. Derksen, *Modal analysis of solar panels using boundary integral equations*, NLR TP 92281 (1992) National Aerospace Laboratory NLR.
8. H. Schippers and J.J. Heijstek, *Modal analysis of solar arrays using hypersingular integral equations*, NLR TP 91267 (1991) National Aerospace Laboratory NLR.
9. W.M. Beltman, P.J.M. van der Hoogt, R.M.E.J. Spiering and H. Tijdeman, *Air loads on solar panels during launch*, Proceedings of the Conference on Spacecraft Structures Materials and Mechanical Testing, March 1996, Noordwijk, The Netherlands.
10. K.M. Liew, K.C. Hung and M.K. Lim, Vibration of Mindlin plates using boundary characteristic orthogonal polynomials, *Journal of Sound and Vibration*, 182 (1995), 77-90.
11. K.C. Park and D.L. Flagg, A symbolic Fourier Synthesis of a one-point integrated quadrilateral plate element, *Comp. Meth. Appl. Mech. Engr.*, 48 (1985), 203-236.
12. H. Schippers, M.G.E. Brand, J.E.J. Maseland and J.J. Heijstek, *On the radar cross section prediction of aerospace platforms*, NLR TP 94486 (1994) National Aerospace Laboratory NLR.
13. J.A. Stratton, *Electromagnetic Theory*, McGraw-Hill, New York (1941).
14. S. Silver, *Microwave Antenne Theory and Design*, Peter Peregrinus, London (1984).
15. T. Abboud and F. Starling, Scattering of an Electromagnetic wave by a Screen, In: M. Costabel, M. Dauge and S. Nicaise (eds.) *Boundary Value Problems and Integral Equations in Nonsmooth Domains*, Lecture Notes in Pure and Applied Mathematics, 167, Marcel Dekker, Inc, New York, Basel, Hong Kong, (1995), pp. 1-17.



16. S.M. Rao and D.R. Wilton and A.W. Glisson, Electromagnetic Scattering by Surfaces of Arbitrary Shape, *IEEE Transactions on Antennas and Propagation*, AP-30 (1982), 409-418.
17. D.S. Wang, Current-Based Hybrid Analysis for Surface-Wave Effects on Large Scatterers, *IEEE Transactions on Antennas and Propagation*, AP-39 (1991), 839-850.
18. A.I. van de Vooren and H.J. van Linde, Numerical calculation of integrals with strongly oscillating integrand, *Math. Comp.* 20 (1966) 232-245.
19. F. Choukroun, *Solveur direct parallèle en acoustique and électromagnétisme, pour les obstacles 3D axisymétriques. Problèmes á hautes fréquences*. Onera N.T. 1997-5 (1997), Onera, Châtillon, France.

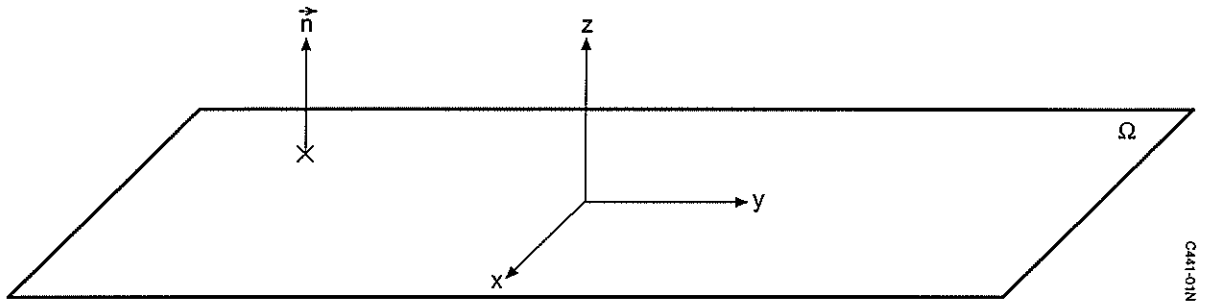


Fig. 1 Solar panel with coordinate system

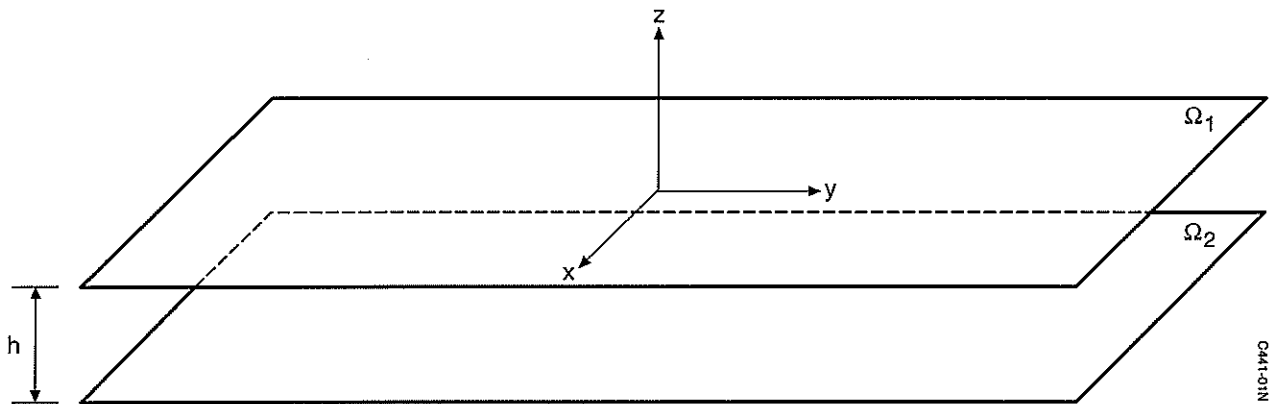


Fig. 2 Two parallel solar panels at a small distance  $h$  apart from each other

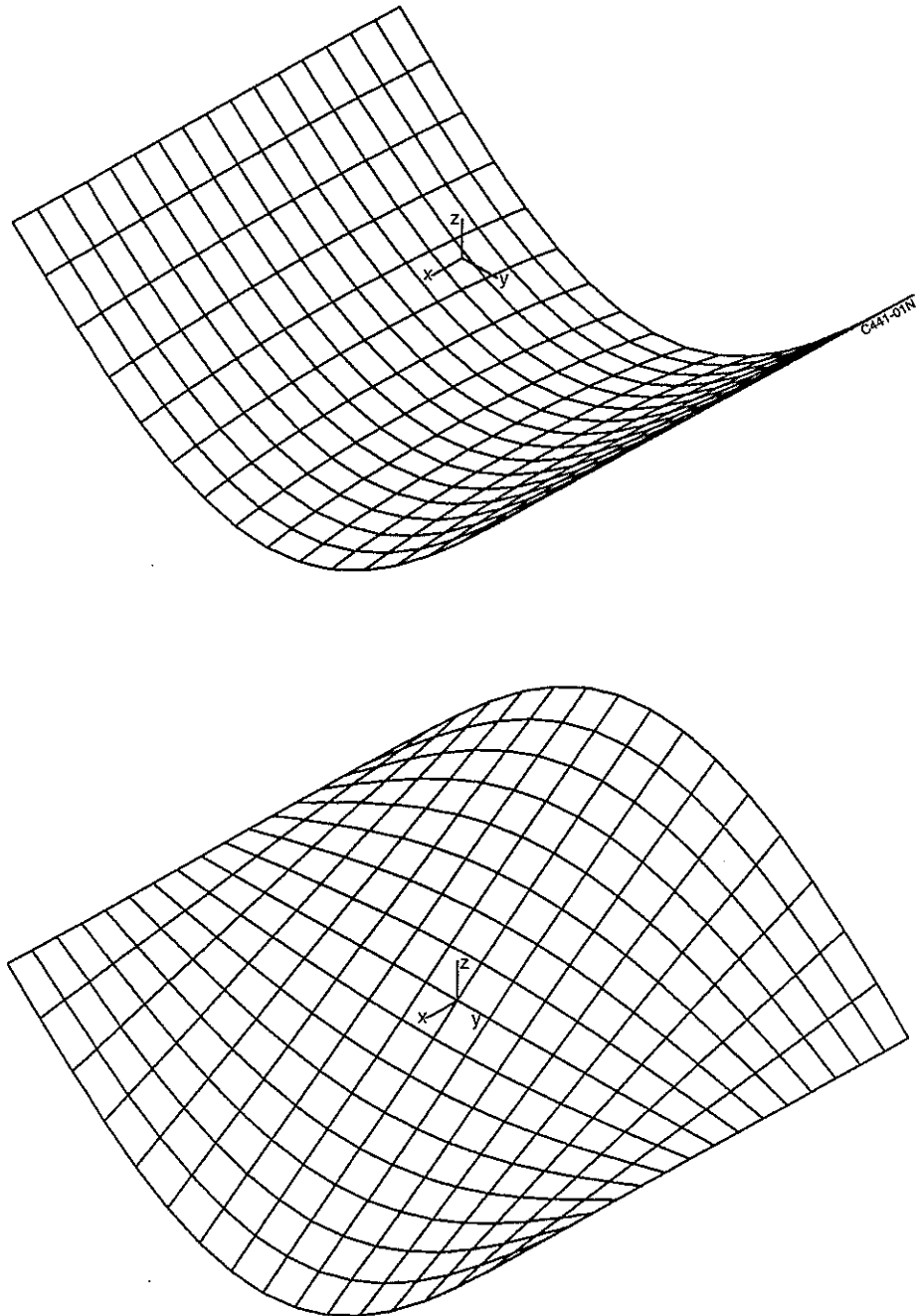


Fig. 3 First two eigenmodes of the solar panel

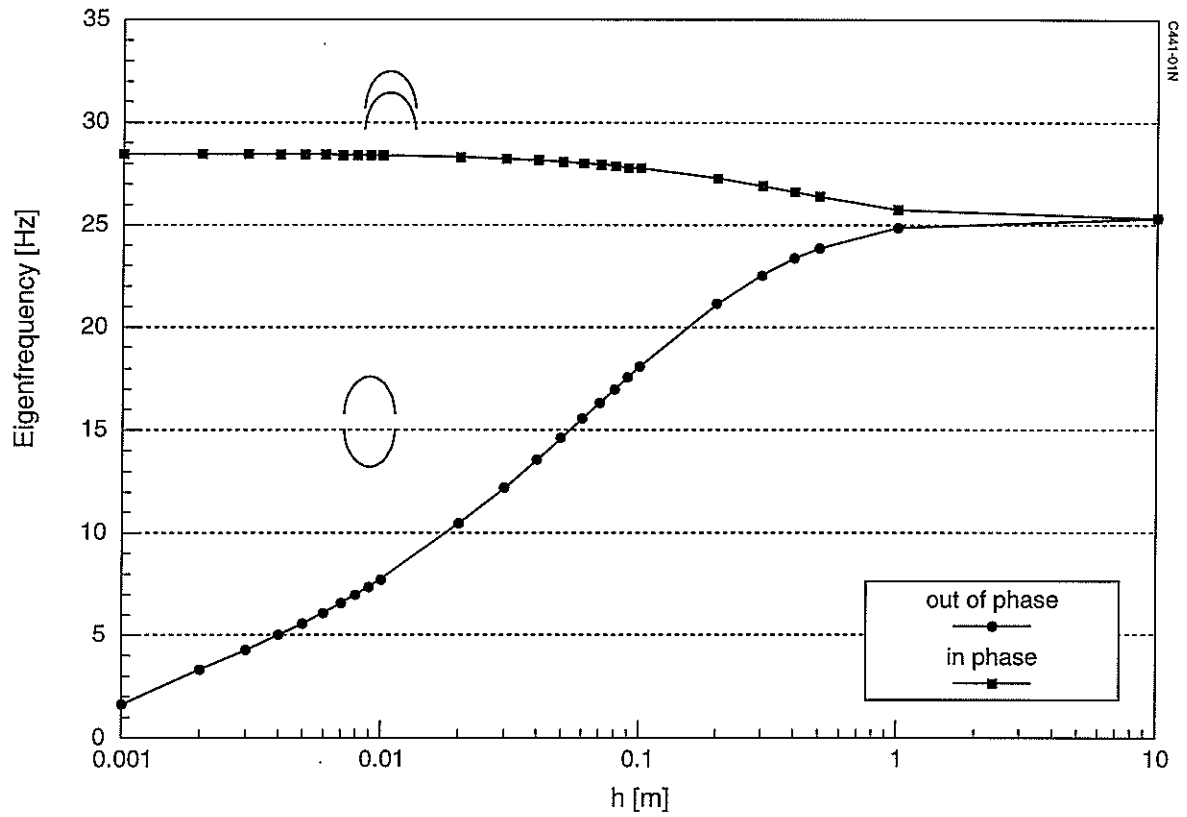


Fig. 4 Two parallel panels: influence panel distance  $h$  on the eigenfrequencies of the first (pair of) eigenmodes

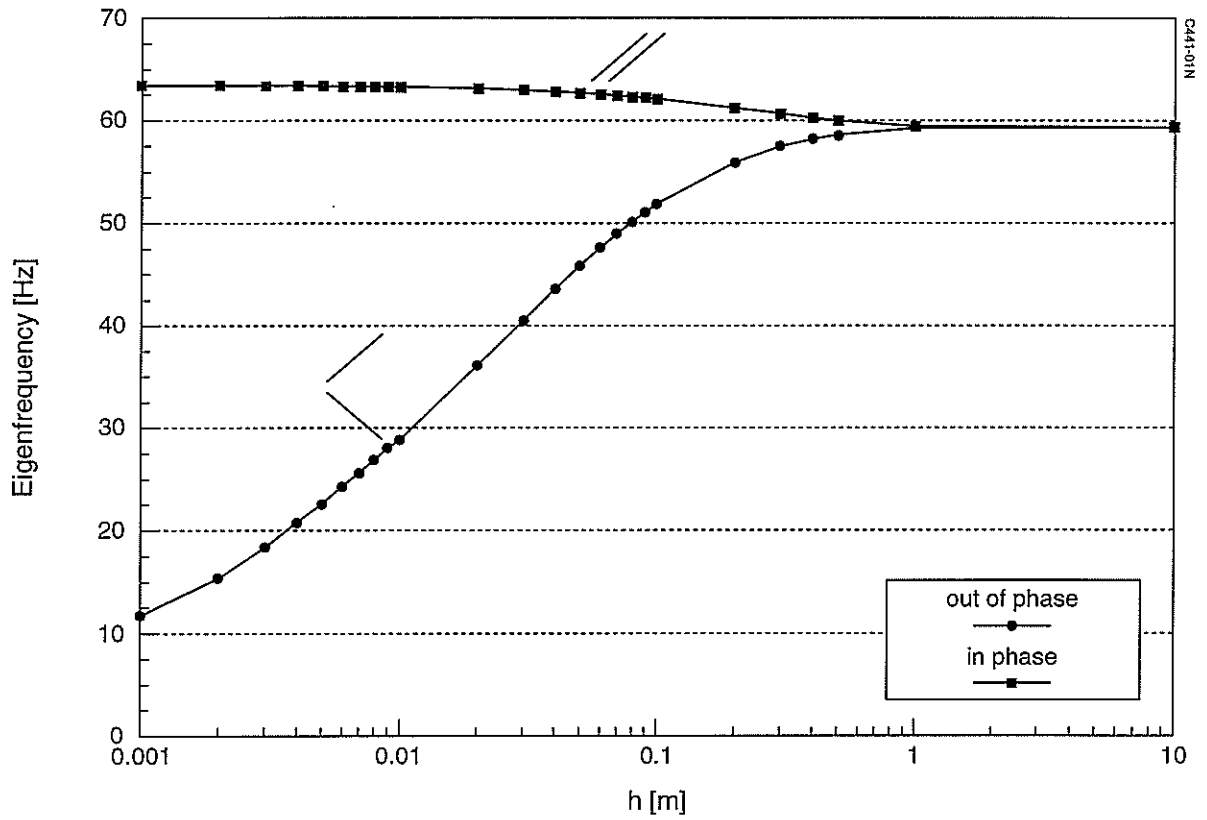


Fig. 5 Two parallel panels: influence panel distance  $h$  on the eigenfrequencies of the second (pair of) eigenmodes

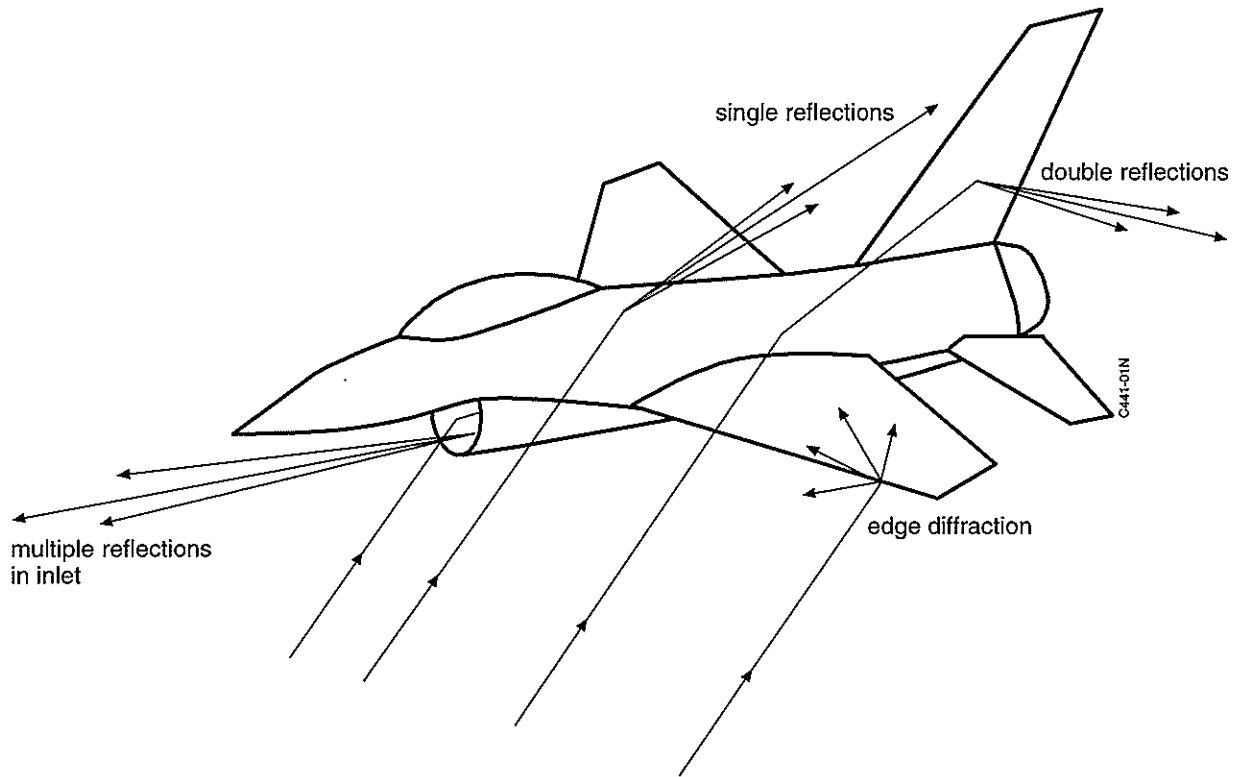


Fig. 6 Scattering mechanisms which contribute to the RCS of a typical fighter aircraft

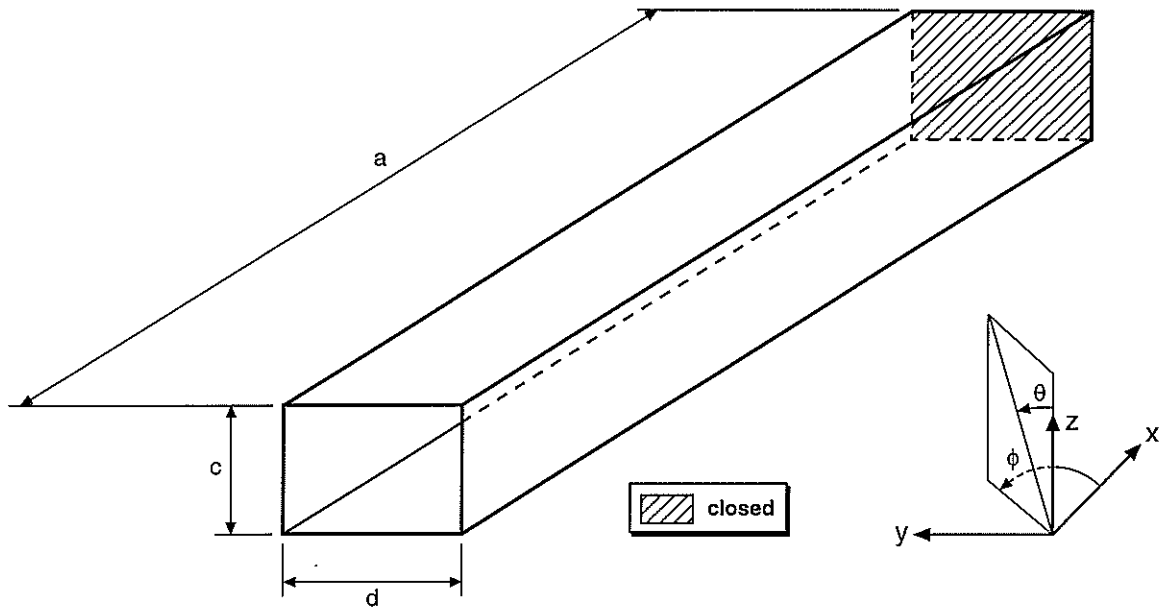


Fig. 7 Rectangular inlet with length  $a = 10\lambda$ , width  $d = 2\lambda$ , height  $c = 2\lambda$

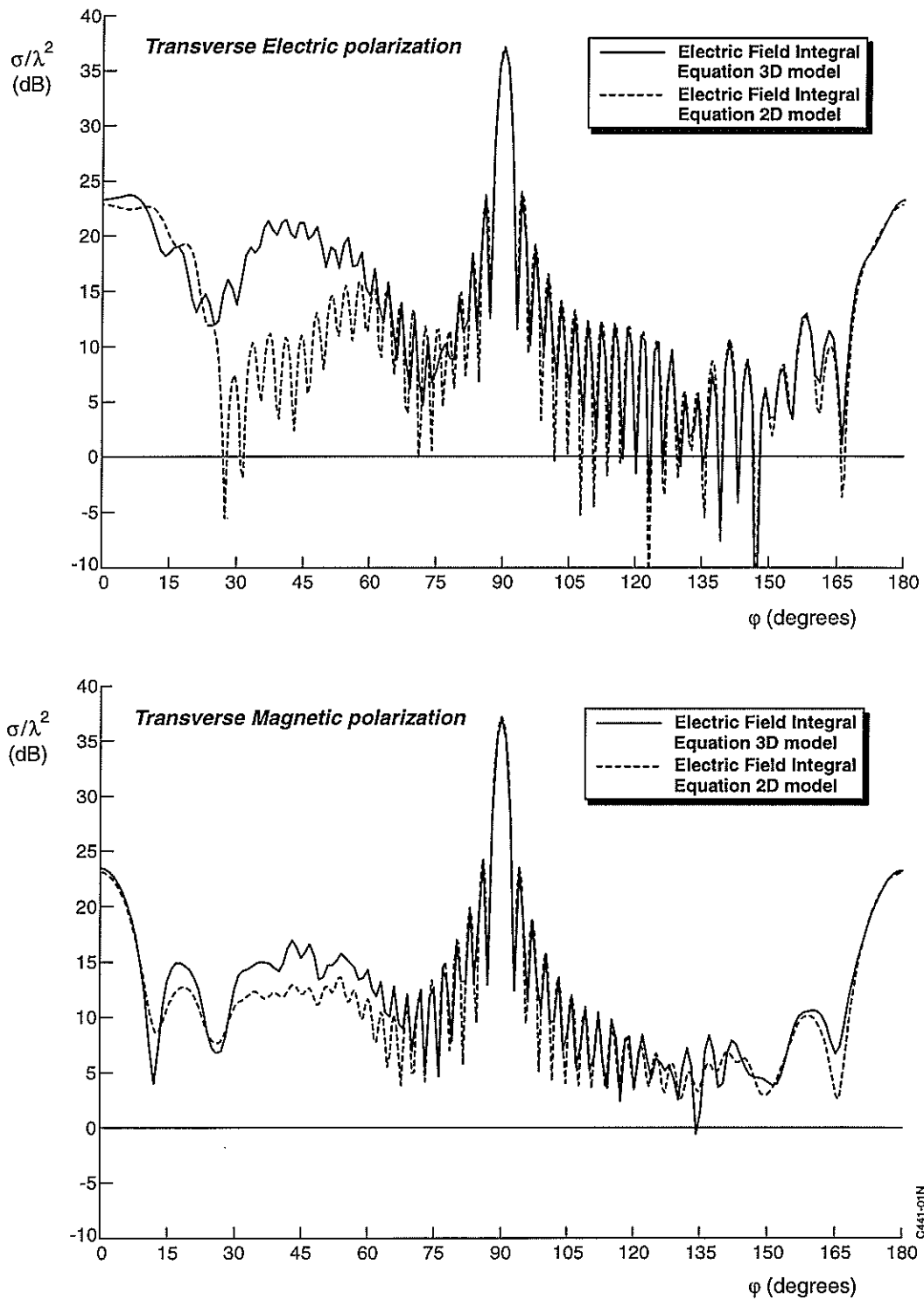


Fig. 8 Comparison of RCS calculations for rectangular inlet in Fig. 7

C441-01N

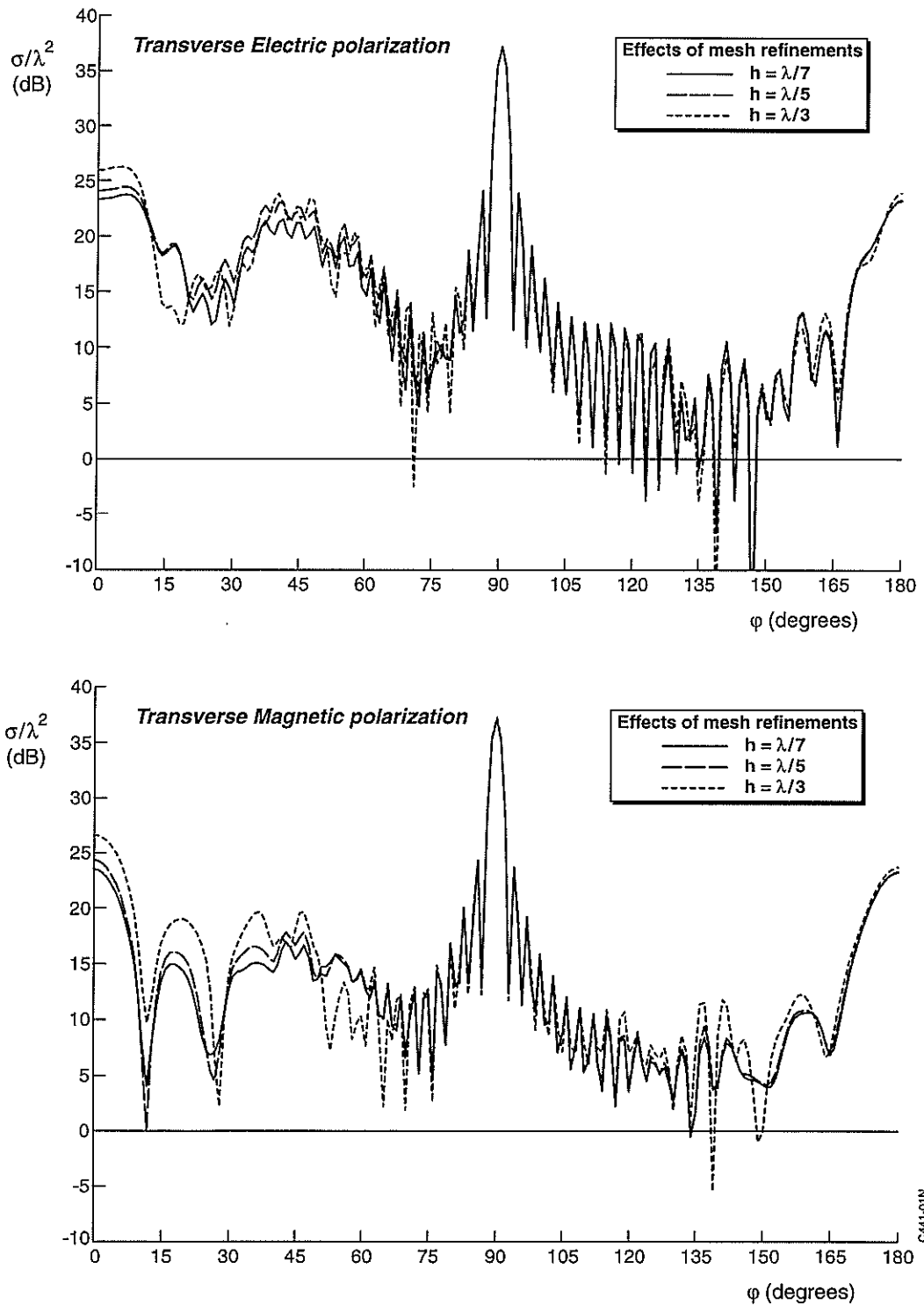


Fig. 9 Assessment of accuracy of RCS calculations for rectangular inlet in Fig. 7

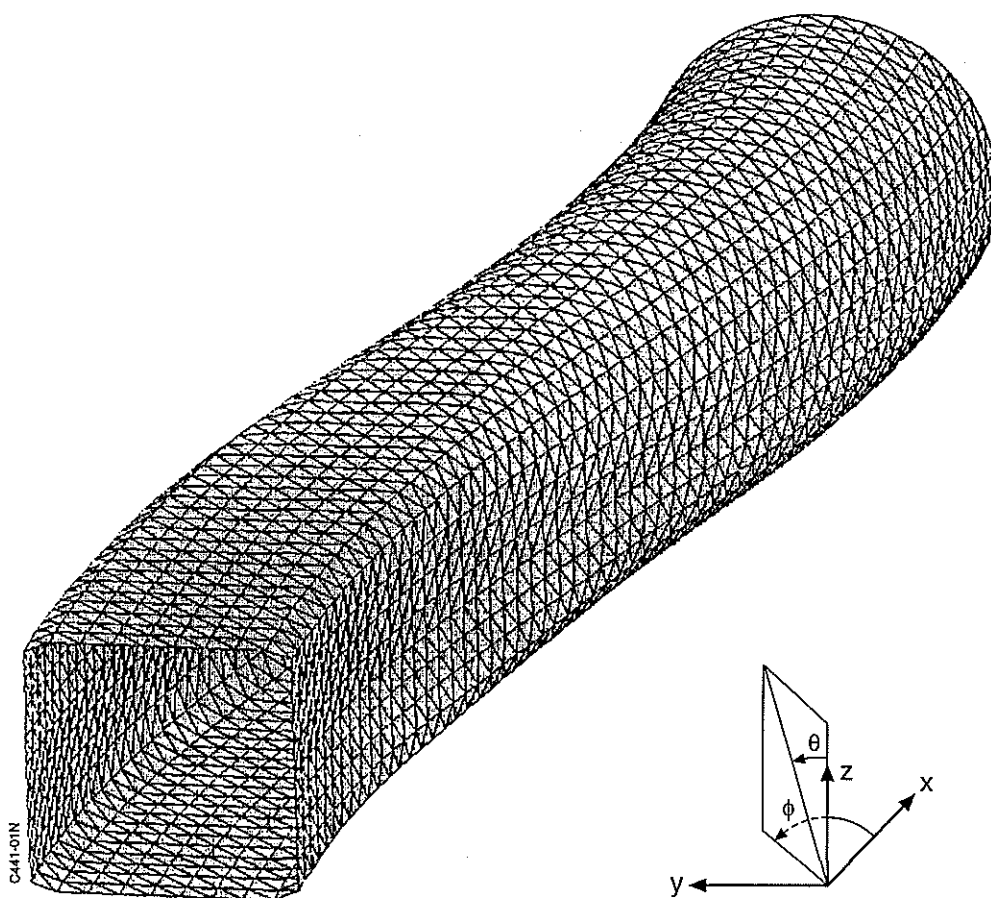


Fig. 8 Comparison of RCS calculations for rectangular inlet in Fig. 7

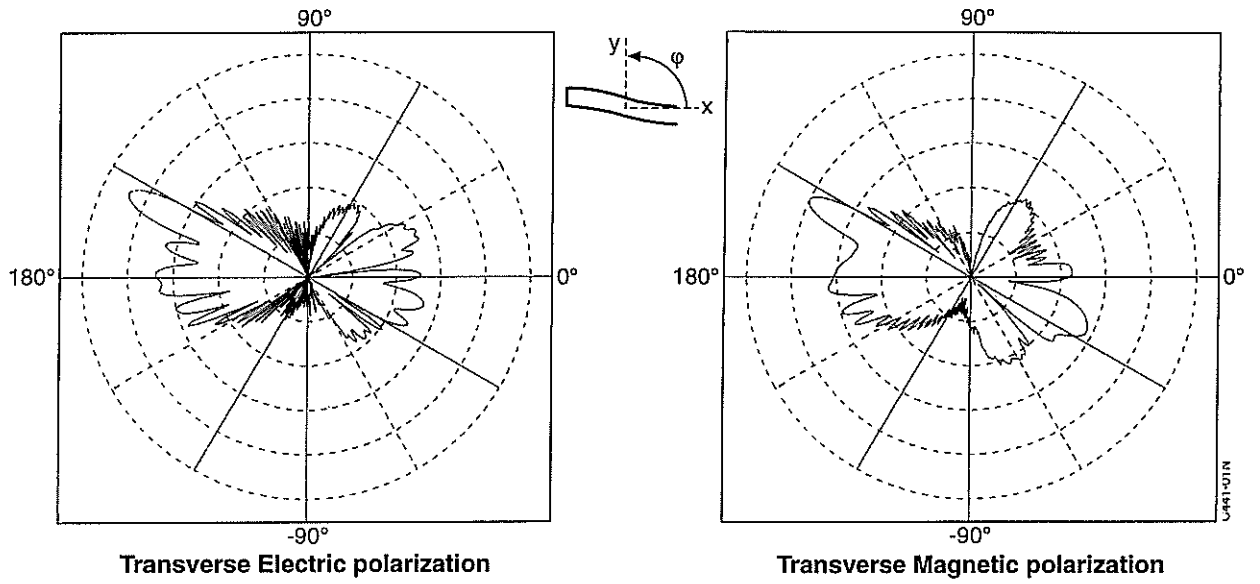


Fig. 11 Calculated bistatic RCS of a curved inlet for an illumination angle  $\phi = -25^\circ$ ,  $\theta = 90^\circ$ , and radar frequency 1.5 GHz